Journal of Power Sources 511 (2021) 230404

Contents lists available at ScienceDirect

Journal of Power Sources

journal homepage: www.elsevier.com/locate/jpowsour

A continuum model of heat transfer in electrical double-layer capacitors with porous electrodes under constant-current cycling

Arpan Kundu [a,1], Laurent Pilon [b], Timothy S. Fisher [b,*]

[a] School of Mechanical Engineering, Purdue University, West Lafayette, IN, USA
[b] Mechanical and Aerospace Engineering Department, University of California, Los Angeles, CA, USA

HIGHLIGHTS

- Supercapacitor electrodes are typically porous.
- Existing theory commonly treats electrodes as flat plates.
- Inclusion of porosity enables accurate temperature prediction in supercapacitors.
- Nondimensionalization enables broad applicability to predict performance.

ARTICLE INFO

Keywords:
Supercapacitors
Porous electrodes
Joule heating
Reversible heating

ABSTRACT

This study presents a theoretical framework to model spatio-temporal heat generation rates and temperature evolution in electrochemical double layer capacitors composed of porous electrodes during constant-current cycling. Expressions for reversible and irreversible heat generation rates are derived based on porous electrode theory. Temperature predictions obtained from the model are found to match experimental trends reported in prior literature as well as quantitative results under various charge/discharge conditions. The model has been applied to investigate the influence of electrode and separator porosity on the operating temperature inside the capacitor during charge/discharge. Furthermore, scaling analysis of the electrothermal model leads to a reduced number of meaningful dimensionless parameters governing electric potential, heat generation rate and temperature rise in the capacitor. We explore the influence of these dimensionless parameters using detailed numerical simulations.

1. Introduction

Electric double-layer capacitors (EDLCs) are primarily used in applications requiring rapid response and long cycle life such as regenerative braking in hybrid electric vehicles [1–4]. They bridge the gap between conventional dielectric capacitors featuring high power densities but low energy densities, and batteries offering high energy densities but low power densities. EDLCs are typically charged/discharged at high current densities, resulting in high volumetric heat generation rates. The heat generation rate depends on numerous factors such as operating conditions, cell design and constituent material properties. Sustained high operating temperatures are known to cause accelerated aging [5–9], high self-discharge rates [5,8,9], electrolyte evaporation [8], and increased cell pressure [8]. The lifetime of a commercial EDLC typically decreases by half for every 10 K rise in average operating temperature [10]. To avoid such harmful effects, temperature rise in EDLCs must be mitigated by developing appropriate cooling and/or load balancing techniques. However, in order to justify the added cost, an accurate estimate of the heat generation rate under various charge/discharge conditions is essential.

In this work, we present a one-dimensional electrothermal model of a commercial EDLC composed of porous electrodes and a binary symmetric electrolyte. Drawing from porous electrode theory, we derive expressions for irreversible and reversible components of the heat generation rate inside the supercapacitor cell as a function of space and time. Detailed numerical simulations of porous electrodes were performed, and the results are compared to experimental results reported in prior literature. Thereafter, scaling analysis is performed to reduce the number of model parameters to a few dimensionless parameters that are important to robust thermal design and management.

* Corresponding author.
E-mail addresses: arpankundu18@gmail.com (A. Kundu), lpilonau@ucla.edu (L. Pilon), tsfisher@ucla.edu (T.S. Fisher).
[1] Currently at Intel Corporation, Chandler, AZ USA.

https://doi.org/10.1016/j.jpowsour.2021.230404
Received 20 April 2021; Received in revised form 16 August 2021; Accepted 17 August 2021

2. Background

2.1. Experimentally observed thermal behavior of supercapacitors

Experimental studies [6,9,11,12] have shown that continuous constant-current cycling of EDLCs (under current $\pm I_s$) result in average temperature increases from cycle to cycle with temperature oscillations superimposed at the cycle frequency. For small operating currents and/or efficient cooling at the device outer surface, the average temperature settles into an oscillatory steady-periodic form. Otherwise, the average temperature rises continuously due to Joule heating. The temperature oscillations are attributed to reversible heating [12].

To gain a better understanding of the electrochemical conversion processes of capacitors, Pascot et al. [13] and Dandeville et al. [14] built a non-adiabatic calorimetric setup to measure temperature evolution in an EDLC (carbon–carbon electrodes) and a hybrid pseudo-capacitor (carbon–MnO_2 electrodes) during galvanostatic cycling. The carbon electrode exhibited exothermic behavior during charging and endothermic behavior during discharging, which is typical of pure EDLCs [9]. By contrast, the MnO_2 electrode exhibited endothermic behavior during charging and exothermic behavior during discharging, which the authors associated with reversible redox reactions occurring during charge/discharge. More recently, Munteshari et al. [15,16] demonstrated experimentally that the heat generation rates depend strongly on the electrode and electrolyte compositions in the EDLCs.

2.2. Thermal modeling of supercapacitors

Most past models either solved the heat diffusion equation [5,6,8,12,17,18] or used the thermal circuit/lumped capacitance approach [5,8] or finite element models. Because such models do not account for reversible heat generation, the resulting temperature profiles do not contain oscillations. The first model to consider EDLC reversible heating was developed by Schiffer et al. [9] based on the entropic effect. The authors considered that the entropy of ions (i) decreased during charging as ions form the electrical double-layer (ordered) and (ii) increased during discharging as the ions return to their original state (disordered). The reversible heat generation rate $\dot{Q}_{rev}$ was expressed as [9],

$$\dot{Q}_{rev} = -T\frac{dS}{dt} = -2\frac{T k_b}{e} ln\left(\frac{V_H}{V_0}\right) I(t) \tag{1}$$

where S is the total entropy of the EDLC system, T is the average cell temperature, and V_H/V_0 represents the factor reduction in ion volume over the charging phase.

More recently, d'Entremont and Pilon [19,20] developed a spatio-temporal model based on first principles by combining the heat diffusion equation with the modified Poisson–Nernst–Planck (MPNP) model to derive analytical expressions for irreversible and reversible heat generation rates in EDLCs comprised of flat plate electrodes, and Janssen and van Roij [21] have provided a rigorous analysis of reversible heating in the slow-charging limit as an improvement to the model of Schiffer et al. [9]. To summarize, past models did not examine the influence of electrode/electrolyte properties and design parameters such as electrode thickness on the volumetric heat generation rate while modeling electrodes as porous objects.

In this work, we address several fundamental questions, namely: (i) What are the individual contributions of electrode and electrolyte to the total heat generation rate inside a porous electrode? (ii) How do operating conditions and supercapacitor design parameters influence temperature evolution? All model parameters are defined in Tables 8 and 9.

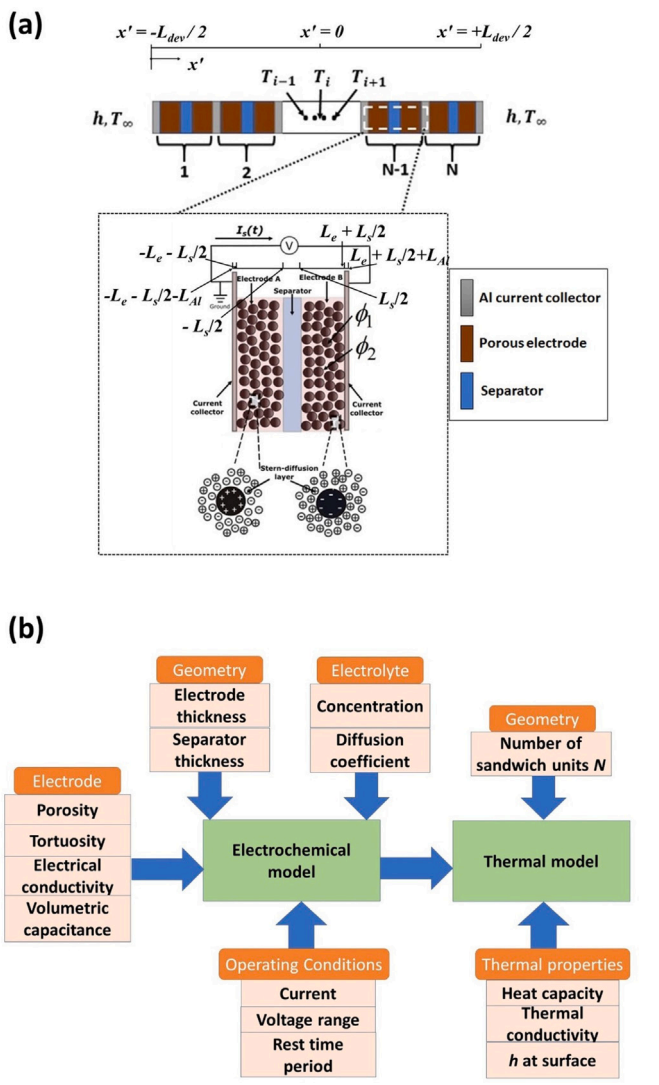

Fig. 1. (a) Schematic of a complete supercapacitor cell consisting of N sandwich units. The magnified view of a single unit shows its major components: (1) aluminum current collector, (2) two porous electrodes each length L_e, composed of activated carbon and (3) a separator of length L_s. (b) An overview of the geometric parameters, operating conditions, and electrode/electrolyte properties that influence temperature evolution in an EDLC cell.

3. Analysis

3.1. Schematics and assumptions

Here, we consider a 1D model of the supercapacitor that neglects heat spreading in the axial direction. Ref. [12] also found that the thermal resistance in the axial direction is much smaller than in the cross-plane direction. Fig. 1a illustrates a one-dimensional cell of thickness L_{dev} consisting of N identical sandwich EDLC units in series. Each unit consists of two identical electrodes of thickness L_e (left denoted as electrode A and right as electrode B) sandwiching a separator of thickness L_s. Each EDLC unit is charged and discharged at a constant current density $I_{im}(t)$ imposed at the right current collector. In galvanostatic charge/discharge measurements, the imposed current density is allowed to vary periodically with time as,

$$I_{im}(t) = \begin{cases} -I_0 & \text{for } 2(n-1)t_c \le t \le 2(n-1)t_c + t_{ch}, \\ +I_0 & \text{for } 2(n-1)t_c + t_{ch} \le t \le 2nt_c. \end{cases} \tag{2}$$

where I_0 is the applied current density in A m^{-2}, n (= 1, 2, 3, …) is the cycle number, and t_c is the cycle period. The cell voltage varies periodically between V_{min} and V_{max}. Here, $\Delta V = V_{max} - V_{min}$ is referred to as the potential window.

The model assumptions are as follows: (1) The electrolyte completely dissociates into its constituent ions. (2) The electrolyte is a 1:1 electrolyte ($z_+ = -z_- = 1$, $c_{+,\infty} = c_{-,\infty} = c_\infty$, $D_{+,\infty} = D_{-,\infty} = D_\infty$). (3) Chemical reactions and ion adsorption due to non-electrostatic forces are absent inside the electrode. (4) Bulk movement of the electrolyte, i.e., advection, is negligible. (5) Steric effects due to ion–ion repulsion are neglected. (6) All electrolyte and electrode properties are independent of temperature. (7) h is constant and independent of surface temperature. (8) Porous electrode theory is sufficient to represent the electrochemical and thermal behavior of the EDLC. (9) D_∞ in the electrolyte is independent of c_∞ and is same in the separator and electrode regions. (10) The electrolyte Seebeck effect of non-isothermal electrolytes is neglected [22]. (11) Electrochemical performance of each unit in the stack is identical.

3.2. Mathematical description

3.2.1. Governing equations for electrochemical transport

The governing equations for electrochemical transport in the sandwich EDLC are obtained from a study by Verbrugge et al. [23]. Conservation of charge requires that the electrical current I_1 in the solid electrode and ionic current I_2 in the electrolyte phase at any location x sum to the imposed current density $I_{im}(t)$,

$$I_{im}(t) = I_1(x,t) + I_2(x,t). \tag{3}$$

The current densities in the solid and liquid phases of the electrode can be expressed by Ohm's law as

$$\begin{aligned} I_1(x,t) &= -\sigma \frac{\partial \phi_1(x,t)}{\partial x}, \\ I_2(x,t) &= -\kappa(c) \frac{\partial \phi_2(x,t)}{\partial x} \end{aligned} \tag{4}$$

where the effective electrical conductivity of the solid phase σ is a constant, and the electrolyte effective ionic conductivity κ is a function of the local ion concentration c and is given by [23]

$$\kappa(c) = \frac{2F^2 Dc(x,t)}{R_u T_0}. \tag{5}$$

The complete set of governing equations for the electrochemical transport variables are displayed in Table 1. Eqs. T1.a and T1.b represent conservation equations for electrode phase potential $\phi_1(x,t)$ and electrolyte phase potential $\phi_2(x,t)$ respectively, while Eqs. T1.c and T1.d represent charge conservation and mass conservation respectively.

The area-normalized capacitance of the sandwich assembly, based on the projected area of the electrodes, C_A (F m^{-2}) is evaluated as

$$C_A = \frac{I_0 t_{dc}}{\Delta V_d} \tag{6}$$

where t_{dc} represents the discharge phase duration and ΔV_d is the cell voltage drop during the discharge phase. The device equivalent series resistance (ESR) is obtained by

$$ESR = \frac{\Delta V_{IR}}{2I_0}, \tag{7}$$

where ΔV_{IR} represents the cell voltage drop at the beginning of discharge phase during the course of galvanostatic cycling.

3.2.2. Governing equations for thermal transport

Because the Biot number is found to be 0.4 (see calculations in Supporting Information), temperature is considered to be non-uniform inside the EDLC device, and is thus a function of both space and time, $T(x,t)$. In the absence of chemical reactions, the energy conservation equation can be expressed as

$$\rho c_p \frac{\partial T}{\partial t} = k \frac{\partial^2 T}{\partial x^2} + \dot{q}_{tot}, \tag{8}$$

where $\dot{q}_{tot}$ is the total volumetric heat generation rate in W m^{-3}, that can be interpreted as

$$\dot{q}_{tot} = \dot{q}_{irr} + \dot{q}_{rev}. \tag{9}$$

The irreversible component is the sum of Joule heating in the solid electrode and in the liquid electrolyte $\dot{q}_{irr} = \dot{q}_{irr,elc} + \dot{q}_{irr,ely}$. Hence, in the electrode regions ($-L_e - L_s/2 \le x \le -L_s/2$ and $L_s/2 \le x \le L_s/2 + L_e$) [20,24]

$$\dot{q}_{irr,elc} = \frac{I_1^2}{\sigma}; \qquad \dot{q}_{irr,ely} = \frac{I_2^2}{\kappa}. \tag{10}$$

In the separator region, the imposed current density $I_{im}(t)$ is transported entirely by the ions through the electrolyte. Thus, for ($-L_s/2 \le x \le L_s/2$) [20],

$$\dot{q}_{irr} = \dot{q}_{irr,ely} = \frac{I_0^2}{\kappa}. \tag{11}$$

An entropy constant β is used to relate $\dot{q}_{rev}$ to the rate of charge accumulation at the electrode/electrolyte interface. Reversible heat generation in the electrode regions ($-L_e - L_s/2 \le x \le -L_e$ and $L_s/2 \le x \le L_s/2 + L_e$) is expressed as

$$\dot{q}_{rev} = \beta \left(aC \frac{\partial(\phi_1 - \phi_2)}{\partial t} \right). \tag{12}$$

whereas it is zero in the separator domain. Details of the derivation of Eq. (12) are provided in the Supporting Information. Using Eq. (T1.c) in Table 1, the reversible heat generation rate in the electrode domains can also be expressed as

$$\dot{q}_{rev} = \beta \frac{\partial I_2}{\partial x}. \tag{13}$$

β formulated in this fashion was determined by Schiffer et al. [9] as 0.101 J C^{-1} by fitting analytical models with experimental measurements. In summary, the heat generation rate $\dot{q}_{tot}$ in the current collector, electrode and separator regions is expressed as

$$\dot{q}_{tot} = \begin{cases} \frac{I_0^2}{\sigma_{Al}}, & -L_{Al} - L_e - L_s/2 \le x \le -L_e - L_s/2 \\ \frac{I_1^2}{\sigma} + \frac{I_2^2}{\kappa} + \beta \frac{\partial I_2}{\partial x}, & -L_e - L_s/2 \le x \le -L_s/2 \quad \& \quad L_s/2 \le x \le L_e + L_s/2 \\ \frac{I_0^2}{\kappa}, & -L_s/2 \le x \le L_s/2 \end{cases} \tag{14}$$

Rewriting the heat diffusion equation, Eq. (8) for each individual domain yields in the current collector domain ($-L_{Al} - L_e - L_s/2 \le x \le -L_e - L_s/2$),

$$(\rho c_p)_{Al} \frac{\partial T}{\partial t} = k_{Al} \frac{\partial^2 T}{\partial x^2} + \frac{I_0^2}{\sigma_{Al}} \tag{15a}$$

In the electrode domains ($-L_e - L_s/2 \le x \le -L_s/2$) and ($L_s/2 \le x \le L_e + L_s/2$), Eq. (8) can be written as

$$(\rho c_p)_{elc,av} \frac{\partial T}{\partial t} = k_{elc,av} \frac{\partial^2 T}{\partial x^2} + \frac{I_1^2}{\sigma} + \frac{I_2^2}{\kappa} + \beta \frac{\partial I_2}{\partial x} \tag{15b}$$

while in the separator domain ($-L_s/2 \le x \le L_s/2$), Eq. (8) can be expressed as

$$(\rho c_p)_{sep,av} \frac{\partial T}{\partial t} = k_{sep,av} \frac{\partial^2 T}{\partial x^2} + \frac{I_0^2}{\kappa}. \tag{15c}$$

Table 1
Electrochemical transport equations for the three regions of a single sandwich unit.

Electrode A $(-L_e - L_s/2 < x < -L_s/2)$	Separator $(-L_s/2 < x < L_s/2)$	Electrode B $(L_s/2 < x < L_s/2 + L_e)$	Eq.
$\frac{\partial \phi_1}{\partial x} = -\frac{I_{im}(t) - I_2}{\sigma}$	–	$\frac{\partial \phi_1}{\partial x} = -\frac{I_{im}(t) - I_2}{\sigma}$	T1.a
$\frac{\partial \phi_2}{\partial x} = -\frac{I_2}{\kappa}$	$\frac{\partial \phi_2}{\partial x} = -\frac{I_2}{\kappa}$	$\frac{\partial \phi_2}{\partial x} = -\frac{I_2}{\kappa}$	T1.b
$\frac{\partial I_2}{\partial x} = aC\frac{\partial(\phi_1 - \phi_2)}{\partial t}$	$I_2 = I_{im}(t)$	$\frac{\partial I_2}{\partial x} = aC\frac{\partial(\phi_1 - \phi_2)}{\partial t}$	T1.c
$\epsilon_e \frac{\partial c}{\partial t} = D_e \frac{\partial^2 c}{\partial x^2} + \frac{aC}{2F}\frac{\partial(\phi_1 - \phi_2)}{\partial t}$	$\epsilon_s \frac{\partial c}{\partial t} = D_s \frac{\partial^2 c}{\partial x^2}$	$\epsilon_e \frac{\partial c}{\partial t} = D_e \frac{\partial^2 c}{\partial x^2} + \frac{aC}{2F}\frac{\partial(\phi_1 - \phi_2)}{\partial t}$	T1.d

3.2.3. Boundary and initial conditions

A summary of the boundary conditions at the current collector and electrode/separator boundaries is displayed in Table 2. Subscripts A, B and s in Eqs. (T2.a–T2.d) represent electrode A, electrode B and the separator respectively. Initially, the supercapacitor is assumed to be in completely discharged state due to which the electrolyte concentration is considered spatially uniform and both the solid phase potential and the liquid phase potential in the electrode are zero throughout.

$$c(x,0) = c_\infty \qquad \text{for} \qquad -L_e - L_s/2 \le x \le L_e + L_s/2. \tag{16a}$$

$$\phi_1(x,0) = \phi_2(x,0) = 0 \qquad \text{for} \qquad -L_e - L_s/2 \le x \le L_e + L_s/2. \tag{16b}$$

The temperature is assumed to be spatially uniform initially,

$$T(x',0) = T_0 \qquad -L_{dev}/2 < x' < L_{dev}/2. \tag{17}$$

where L_{dev} is the thickness of the device which consists of N number of sandwich units. The boundary condition at the left end of the device domain has been considered as,

$$-k_{Al}\frac{\partial T}{\partial x'}|_{x'=0} = h(T_\infty - T(x'=0,t)). \tag{18}$$

Similarly, the right end boundary condition is

$$-k_{Al}\frac{\partial T}{\partial x'}|_{x'=L_{dev}} = h(T(x'=L_{dev},t) - T_\infty). \tag{19}$$

Here, the ambient temperature T_∞ is considered to be identical to the initial temperature T_0.

3.2.4. Constitutive relationships

The physical properties in the electrode and separator domains are calculated using a weighted average,

$$\begin{aligned} M_{elc,av} &= \epsilon_e M_{ely} + (1-\epsilon_e)M_{elc} \\ M_{sep,av} &= \epsilon_s M_{ely} + (1-\epsilon_s)M_{sep} \end{aligned} \tag{20}$$

where ϵ_e and ϵ_s represent electrode and separator porosity. The property M stands for density ρ, thermal conductivity k and thermal diffusivity α. The number of layers varies with device size.

In this study, N number of sandwich units are stacked in series to construct a device (schematic shown in Fig. 1a), which is very similar in construction to the real-world supercapacitor device displayed in Figure S1a. Here, N is assumed to be 50 corresponding to a total device thickness of 7.25 mm. Because the thermal resistance in the axial direction is much smaller than in the radial direction [12], the device can be represented by a 1D model.

3.2.5. Dimensional analysis

The electrothermal model described by governing equations listed in Table 1 and Eq. (8) and the associated initial and boundary conditions listed in Table 2 and Eqs. (16)–(19) contain 29 dimensional variables L_e, L_s, L_{Al}, L_{dev}, ϕ_1, ϕ_2, I_0, I_2, I_{im}, σ, σ_{Al}, F, R_u, T_0, D_e, c, c_∞, aC, t, x, $(\rho c_p)_{elc,av}$, $(\rho c_p)_{sep,av}$, $(\rho c_p)_{Al}$, $k_{elc,av}$, $k_{sep,av}$, k_{Al}, h, β and T. Following past studies [25,26], application of Buckingham-Pi analysis to our electrothermal model yielded the non-dimensional space and time variables given by Eq. (21a), 18 other independent dimensionless variables given by Eq. (21b), and 5 dependent dimensionless variables given by Eq. (21c).

$$x^* = \frac{x}{L_e}, \quad t^* = \frac{tD_e}{L_e^2}. \tag{21a}$$

$$\begin{aligned} &\epsilon_e, \quad \epsilon_s, \quad L_s^* = \frac{L_s}{L_e}, \quad L_{Al}^* = \frac{L_{Al}}{L_e}, \quad L_{dev}^* = \frac{L_{dev}}{L_e}, \\ &I_{im}^* = \frac{I_{im}}{I_0}, \quad (\rho c_p)_{Al}^* = \frac{(\rho c_p)_{Al}}{(\rho c_p)_{elc,av}}, \quad (\rho c_p)_{sep,av}^* = \frac{(\rho c_p)_{sep,av}}{(\rho c_p)_{elc,av}}, \\ &k_{Al}^* = \frac{k_{Al}}{k_{elc,av}}, \quad k_{sep,av}^* = \frac{k_{sep,av}}{k_{elc,av}}, \quad \sigma^* = \frac{\sigma}{\sigma_{Al}}, \\ &\Pi_1 = \frac{I_0 F L_e}{\sigma R_u T_0}, \quad \Pi_2 = \frac{I_0 L_e}{2F D_e c_\infty}, \quad \Pi_3 = \frac{aCD_e}{\sigma}, \quad \Pi_4 = \frac{k_{elc,av}}{(\rho c_P)_{elc,av} D_e}, \\ &\Pi_5 = \frac{I_0 L_e R_u}{F D_e (\rho c_P)_{elc,av}}, \quad \Pi_6 = \frac{\beta F}{R_u T_0}, \quad \Pi_7 = \frac{hL_e}{k_{Al}}. \end{aligned} \tag{21b}$$

$$\phi_1^* = \frac{\phi_1 F}{R_u T_0}, \quad \phi_2^* = \frac{\phi_2 F}{R_u T_0}, \quad I_2^* = \frac{I_2}{I_0}, \quad c^* = \frac{c}{c_\infty}, \quad T^* = \frac{T - T_0}{T_0}. \tag{21c}$$

Here, the position vector x is scaled by the electrode thickness L_e while the solid phase and liquid phase potentials are scaled by the thermal voltage $R_u T_0/F$ which represents the voltage inducing electrical energy equivalent to the thermal energy for an ion of valency 1 at ambient temperature T_0. The time t is scaled by the characteristic time for ion diffusion across the length of the porous electrode estimated as $\tau_d = L_e^2/D_e$. The imposed current density I_{im}, solid phase current density I_1, liquid phase current density I_2 are scaled by the magnitude of applied current density I_0. Consequently, the dimensionless imposed current density I_{im}^* takes a value of -1 during charging and $+1$ under discharge. Finally, the ion concentration $c(x,t)$ and temperature change $T(x,t) - T_0$ are scaled by the bulk ion concentration c_∞ and initial temperature T_0 respectively. The resulting dimensionless governing equations for the electrochemical model are shown in Table 3, and the associated dimensionless boundary conditions are documented in Table 4.

The dimensionless number Π_1 scales the voltage across the length of the electrode in the solid phase $I_0 L_e/\sigma$ by the thermal voltage $R_u T_0/F$. Similarly, the dimensionless number Π_2 scales the voltage across the length of the electrode in the liquid phase $I_0 L_e/\kappa_e$ by the thermal voltage $R_u T_0/F$. Π_3 denotes the dimensionless volumetric capacitance of the electrode. Π_4 is equal to the effective Lewis number for the electrode which can be interpreted as the ratio of the characteristic time for ion diffusion $\tau_d = L_e^2/D_e$ to that for heat diffusion $\tau_{th} = L_e^2/\alpha_{elc,av}$ in the electrode. The dimensionless number Π_5 represents the ratio of the characteristic volumetric heat capacity $C_d = I_0 L_e R_u/F D_e$ to that of the electrode $(\rho c_p)_{elc,av}$. Similarly, Π_6 scales the reversible heat coefficient β to the thermal voltage, and Π_7 is the effective Biot number considering the characteristic length to be the electrode thickness L_e. The dimensionless energy conservation equation becomes:

$$\frac{\partial T^*}{\partial t^*} = Fo_{Al}\frac{\partial^2 T^*}{\partial x^{*2}} + \frac{\Pi_1 \Pi_5}{(\rho c_P)_{Al}^*}\sigma^* \tag{22a}$$

Table 2
Boundary conditions at interfaces between regions of a single sandwich unit.

Current collector interface ($x = -L_e - L_s/2$)	Electrode A-separator interface ($x = -L_s/2$)	Electrode B-separator interface ($x = L_s/2$)	Current collector interface ($x = L_e + L_s/2$)	Eq.
$\phi_1\|_A = 0$	$\frac{\partial\phi_1}{\partial x}\|_A = -\frac{I_{im}(t)-I_2}{\sigma}$	$\frac{\partial\phi_1}{\partial x}\|_B = -\frac{I_{im}(t)-I_2}{\sigma}$	$\frac{\partial\phi_1}{\partial x}\|_B = -\frac{I_{im}(t)-I_2}{\sigma}$	T2.a
$\frac{\partial\phi_2}{\partial x}\|_A = -\frac{I_2\|_A}{\kappa}$	$[\kappa\frac{\partial\phi_2}{\partial x}]_A = [\kappa\frac{\partial\phi_2}{\partial x}]_s$	$[\kappa\frac{\partial\phi_2}{\partial x}]_s = [\kappa\frac{\partial\phi_2}{\partial x}]_B$	$\frac{\partial\phi_2}{\partial x}\|_B = -\frac{I_2\|_B}{\kappa}$	T2.b
$I_2\|_A = 0$	$I_2\|_A = I_{im}(t)$	$I_2\|_B = I_{im}(t)$	$I_2\|_B = 0$	T2.c
$\frac{\partial c}{\partial x}\|_A = 0$	$D\frac{\partial c}{\partial x}\|_A = D\frac{\partial c}{\partial x}\|_s$	$D\frac{\partial c}{\partial x}\|_s = D\frac{\partial c}{\partial x}\|_B$	$\frac{\partial c}{\partial x}\|_B = 0$	T2.d

in the current collector domain ($-L_{Al}^* - 1 - L_s^*/2 \le x^* \le -1 - L_s^*/2$). Fo_{Al} can be represented by $\frac{k_{Al}^*}{(\rho c_P)_{Al}^*}\Pi_4$. Similarly,

$$\frac{\partial T^*}{\partial t^*} = Fo_{elc,av}\frac{\partial^2 T^*}{\partial x^{*2}} + \Pi_1\Pi_5(I_{im}^* - I_2^*)^2 + \Pi_2\Pi_5\frac{I_2^{*2}}{c^*} + \Pi_5\Pi_6\frac{\partial I_2^*}{\partial x^*} \quad (22b)$$

in the electrode domains ($-1 - L_s^*/2 \le x^* \le -L_s^*/2$) and ($L_s^*/2 \le x^* \le 1 + L_s^*/2$). Here, $Fo_{elc,av} = \Pi_4$. Similarly,

$$\frac{\partial T^*}{\partial t^*} = Fo_{sep,av}\frac{\partial^2 T^*}{\partial x^{*2}} + \frac{1}{(\rho c_p)_{sep,av}^*}\frac{\Pi_2\Pi_5}{c^*} \quad (22c)$$

in the separator domain ($-L_s^*/2 \le x^* \le L_s^*/2$). Here, $Fo_{sep,av} = \frac{k_{sep,av}^*}{(\rho c_P)_{sep,av}^*}\Pi_4$.

The boundary condition at the left end boundary ($x'^* = -L_{dev}^*/2$) is given by,

$$\frac{\partial T^*}{\partial x'^*}|_{-L_{dev}^*/2} = \Pi_7 T^*_{-L_{dev}^*/2}. \quad (23)$$

Similarly, the boundary condition at the right end boundary ($x'^* = L_{dev}^*/2$) is given by,

$$\frac{\partial T^*}{\partial x'^*}|_{L_{dev}^*/2} = -\Pi_7 T^*_{L_{dev}^*/2}. \quad (24)$$

3.2.6. Method of solution

The dimensionless governing equations along with associated boundary conditions shown in Tables 3 and 4 respectively were solved with uniform mesh size in both electrode and separator regions to compute the electrochemical transport variables ϕ_1^*, ϕ_2^*, I_2^* and c^*, while Eqs. (22), (23) and (24) were used to determine T^*. The results depend only on the 18 independent dimensionless numbers defined in Eq. (21a) and the ratio of porosity $\frac{\epsilon_e}{\epsilon_s}$. The obtained dimensionless variables were scaled to dimensional variables using equations described in Eq. (21). The evolution in device centerline temperature ($x = 0$) was characterized by two parameters: (i) the time-averaged irreversible temperature rise T_{irr}^K

$$T_{irr}^K = \frac{\int_{(K-1)t_c}^{Kt_c} T(0,t)dt}{t_c} \quad (25)$$

and the temperature oscillation amplitude ΔT_{rev}^K expressed as:

$$\Delta T_{rev}^K = T[0,(K-1)t_c + t_{ch}] - T[0,Kt_c]. \quad (26)$$

Also, we define the spatially and temporally averaged heat generation rate $\bar{\dot{q}}_i$ (W m^{-3}) as:

$$\bar{\dot{q}}_i = \frac{1}{(2L_e + L_s)(t_{ch} + t_{dc})}\int_0^{t_{ch}+t_{dc}}\int_0^{(2L_e+L_s)} \dot{q}_i(x,t)dxdt \quad (27)$$

4. Results and discussion

Simulations were performed for the set of operating and design parameters shown in Table 8.

4.1. Dimensional model analysis

Fig. 2(a) shows that for an operating current density $I_0 = 50$ A m^{-2}, the cell voltage rises linearly from 0 to 2.7 V during charging while in the discharge phase, it first undergoes a drop of 0.23 V (corresponding to a specific internal resistance value of 2.3 mΩ m^2) and then declines linearly to 0 V. The cycle period t_c of 102 s is comparable to that observed for a commercial EDLC composed of porous electrodes [27]. Fig. 2(b) shows the spatial variation of solid phase current density I_1 and liquid phase current density I_2 during charging at $t = 0.25t_c$. At any location, $I_1 + I_2 = I_{im}$. Furthermore, both I_1 and I_2 are symmetric about the centerline, which is representative of pure double-layer behavior.

The spatial variation of volumetric heat generation rates $\dot{q}_{irr,elc}$, $\dot{q}_{irr,ely}$, $\dot{q}_{irr}$, $\dot{q}_{rev}$ and $\dot{q}_{tot}$ halfway into the charge phase ($t = 0.25t_c$) and halfway into the discharge phase ($t = 0.75t_c$) are shown in Fig. 2(c) and (d) respectively. The spatial variation of both $\dot{q}_{irr,ely}$ and $\dot{q}_{irr,elc}$ can be observed to be greater within the electrodes compared to within the separator. The large spatial variation can be attributed to spatially varying I_1 and I_2 as shown in Fig. 2(b). In summary, the total heat generation rate varies considerably in space during charge/discharge. The electrochemical performance and temperature evolution of the EDLC device was studied for different values of operating current density I_0. Fig. 2(e) shows the cell potential $V_{cell}(t) = \phi_1(2L_e + L_s, t) - \phi_1(0, t)$ as a function of time t for $I_0 = 30$, 50 and 70 A m^{-2}. The variation of device centerline temperature $T(0, t_0)$ are shown in Fig. 2(f) for $I_0 = 30$, 50 and 70 A m^{-2}, while the corresponding temperature profiles as a function of location inside the device is shown in Figure S5. At all I_0, the temperature rises rapidly in the beginning before reaching oscillatory steady-state at which point the convective heat loss equals the irreversible heat generation rate. However, at low I_0, the system reaches steady state temperature much quicker.

4.1.1. Comparison of temperature evolution with experimental measurements

Fig. 3a displays the experimental temperature measurements obtained on a commercially available 350 F EDLC charged/discharged galvanostatically at ±15 A and cooled by natural convection on the external surface.

Fig. 3(b) shows the numerical results obtained from the present model for $I_0 = 50$ A m^{-2} and $h = 20$ W m^{-2} K^{-1}. 15 A current applied to charge/discharge the commercial BCA350F supercapacitor studied in Ref. [12] corresponds to an operating current density of 50 A m^{-2} as shown in Section 1.3 of the Supporting Information. A comparison of Fig. 3(a) and (b) demonstrates that the predicted temperature evolution closely resembles past measurements on commercial EDLCs both qualitatively as well as quantitatively. At all locations, the overall temperature rises rapidly from cycle to cycle followed by gradual saturation. Furthermore, temperature oscillations are superimposed onto the average temperature profile as a consequence of reversible heat generation. At saturation, the total heat generation rate inside the device equals heat dissipation rate to the ambient. The temperature oscillations occurring at the cycle frequency can be attributed to reversible heat generation. The oscillation amplitude is predicted to be around 1.15 °C, which is close to 0.9 °C recorded by Schiffer [9] on the surface of a commercial 5000 F Nesscap EDLC during galvanostatic cycling in a voltage window of 0.5 and 2.5 V. Although the temperature profiles for porous electrodes resemble those of planar electrodes [19,20], temperature oscillations are much larger than those

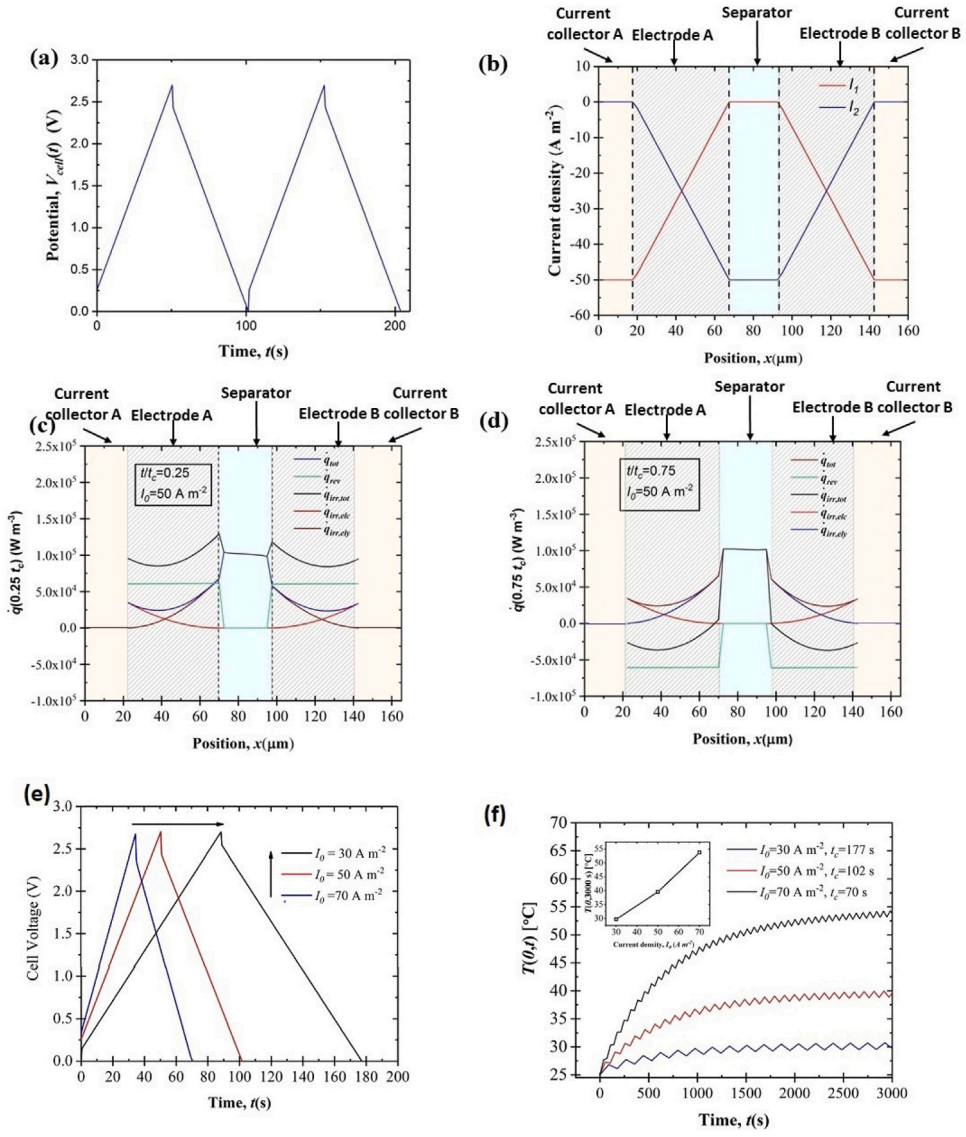

Fig. 2. (a) Cell voltage $V_{cell}(t) = \phi_1(2L_c + L_s, t) - \phi_1(0, t)$ as a function of time during two consecutive charge/discharge cycles for a constant operating current density I_0 = 50 A m^{-2}. The device operates in the voltage range of 0 to 2.7 V. (b) Spatial variation of solid phase current density I_1 and liquid phase current density I_2 halfway into the charging phase at $t = 0.25t_c$. Predicted heat generation rates $\dot{q}_{irr,elc}(x,t)$, $\dot{q}_{irr,ely}(x,t)$, $\dot{q}_{irr}(x,t)$, $\dot{q}_{rev}(x,t)$ and $\dot{q}_{tot}(x,t)$ as function of location x at dimensionless time (c) t/t_c = 0.25 and (d) t/t_c = 0.75 for I_0 = 50 A m^{-2}. (e) Galvanostatic charge/discharge profiles at operating current density I_0 = 30, 50 and 70 A m^{-2} in the voltage range of 0–2.7 V. (f) Predicted device centerline temperature $T(0,t)$ as a function of time t for continuous galvanostatic cycling at I_0 = 30, 50 and 70 A m^{-2}. The inset shows the device centerline temperature at $t = t_0$ (3000 s), $T(0,t_0)$ as a function of I_0.

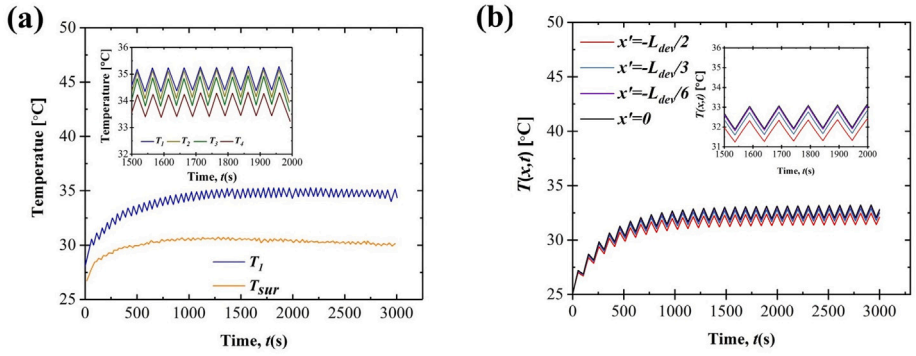

Fig. 3. (a) Thermocouple temperature measurements at different positions of a BCAP350 F EDLC cycled at ± 15 A plotted as a function of time t (reproduced from Figure 10(a) of Ref. [12]). The inset shows a magnified view of the temperature profiles (reproduced from Figure 10(b) of Ref. [12]). In the figure, T_{sur} represents the surface temperature, while T_1, T_2, T_3 and T_4 represent temperature at different radial positions proceeding in the radially outward direction from the center. (b) Numerically predicted temperature evolution with time at positions $x = 0$, $x = L_{dev}/6$, $x = L_{dev}/3$ and $x = L_{dev}/2$ for I_0 = 50 A m^{-2} and h = 20 W m^{-2} K^{-1}. The inset shows a magnified view of the temperature profiles in the time range of 1500 and 2000 s.

Table 3
Normalized field equations in the three regions of a single sandwich unit.

Left electrode $(-1-L_s^*/2) < x^* < -L_s^*/2$	Separator $-L_s^*/2 < x^* < L_s^*/2$	Right electrode $L_s^*/2 < x^* < (1+L_s^*/2)$
$\frac{\partial \phi_1^*}{\partial x^*} = -\Pi_1(I_{im}^* - I_2^*)$	–	$\frac{\partial \phi_1^*}{\partial x^*} = -\Pi_1(I_{im}^* - I_2^*)$
$\frac{\partial \phi_2^*}{\partial x^*} = -\Pi_2 \frac{I_2^*}{c^*}$	$\frac{\partial \phi_2^*}{\partial x^*} = -\Pi_2 (\frac{\epsilon_s}{\epsilon_s})^{3/2} \frac{I_2^*}{c^*}$	$\frac{\partial \phi_2^*}{\partial x^*} = -\Pi_2 \frac{I_2^*}{c^*}$
$\frac{\partial I_2^*}{\partial x^*} = \frac{\Pi_3}{\Pi_1} \frac{\partial(\phi_1^* - \phi_2^*)}{\partial t^*}$	$I_2^* = I_{im}^*$	$\frac{\partial I_2^*}{\partial x^*} = \frac{\Pi_3}{\Pi_1} \frac{\partial(\phi_1^* - \phi_2^*)}{\partial t^*}$
$\epsilon_e \frac{\partial c^*}{\partial t^*} = \frac{\partial^2 c^*}{\partial x^{*2}} + \frac{\Pi_2 \Pi_3}{\Pi_1} \frac{\partial(\phi_1^* - \phi_2^*)}{\partial t^*}$	$\epsilon_e \frac{\partial c^*}{\partial t^*} = (\frac{\epsilon_s}{\epsilon_e})^{1/2} \frac{\partial^2 c^*}{\partial x^{*2}}$	$\epsilon_e \frac{\partial c^*}{\partial t^*} = \frac{\partial^2 c^*}{\partial x^{*2}} + \frac{\Pi_2 \Pi_3}{\Pi_1} \frac{\partial(\phi_1^* - \phi_2^*)}{\partial t^*}$

Table 4
Normalized boundary conditions at interfaces between regions of a single sandwich unit.

Current collector interface $(x^* = -1 - L_s^*/2)$	Electrode–separator interface $(x^* = -L_s^*/2)$	Electrode–separator interface $(x^* = L_s^*/2)$	Current collector interface $(x^* = 1 + L_s^*/2)$
$\phi_1^* = 0$	$\frac{\partial \phi_1^*}{\partial x^*}\|_L = -\Pi_1(I_{im}^* - I_2^*)$	$\frac{\partial \phi_1^*}{\partial x^*}\|_R = -\Pi_1(I_{im}^* - I_2^*)$	$\frac{\partial \phi_1^*}{\partial x^*}\|_R = -\Pi_1(I_{im}^* - I_2^*)$
$\frac{\partial \phi_2^*}{\partial x^*} = -\Pi_2 \frac{I_2^*}{c^*}$	$c^* \frac{\partial \phi_2^*}{\partial x^*}\|_L = (\frac{\epsilon_s}{\epsilon_e})^{3/2} c^* \frac{\partial \phi_2^*}{\partial x^*}\|_R$	$(\frac{\epsilon_s}{\epsilon_e})^{3/2} c^* \frac{\partial \phi_2^*}{\partial x^*}\|_L = c^* \frac{\partial \phi_2^*}{\partial x^*}\|_R$	$\frac{\partial \phi_2^*}{\partial x^*} = -\Pi_2 \frac{I_2^*}{c^*}$
$I_2^* = 0$	$I_2^* = I_{im}^*$	$I_2^* = I_{im}^*$	$I_2^* = 0$
$\frac{\partial c^*}{\partial x^*} = 0$	$\frac{\partial c^*}{\partial x^*}\|_L = (\frac{\epsilon_s}{\epsilon_e})^{3/2} \frac{\partial c^*}{\partial x^*}\|_R$	$(\frac{\epsilon_s}{\epsilon_e})^{3/2} \frac{\partial c^*}{\partial x^*}\|_L = \frac{\partial c^*}{\partial x^*}\|_R$	$\frac{\partial c^*}{\partial x^*} = 0$

for planar electrodes because of the higher reversible heat generation rate caused by larger surface-to-volume ratio. These results highlight the capabilities and advantages of the present electrothermal model for porous electrodes, as it can predict realistic temperature profiles in a computationally efficient manner based on coupled electrochemical and transport phenomena within the EDLC devices and without relying on empirical fitting parameters.

4.1.2. Influence of operating conditions and device design parameters

Fig. 4 illustrates the change in device electrochemical characteristics and temperature rise during galvanostatic cycling as a result of independent variation in electrode porosity ϵ_e and separator porosity ϵ_s. As shown in Fig. 4(a) and (c), the device centerline temperature rises more significantly with time for smaller ϵ_e corresponding to lower effective ionic conductivity and larger volumetric heat generation rate in the electrode region as illustrated by Eqs. (5) and (10). The device centerline temperature at the end of 3000 s decreases from 100 °C to 40 °C as a result of increase in ϵ_e from 0.2 to 0.9. Furthermore, with rise in ϵ_e, the area-normalized device capacitance C_A increases rapidly at the beginning and then reaches saturation as illustrated in Fig. 4(c) which can be attributed to higher effective contact surface area for the electrolyte. The influence of separator porosity ϵ_s on the device centerline temperature and device capacitance is shown in Fig. 4(b) and (d). The device centerline temperature decreases from 70 °C to 36 °C as a result of change in ϵ_s from 0.2 to 0.9 due to a resulting increase in effective ionic conductivity in the separator region. However, the device capacitance C_A remains unchanged at 1020 F m^{-2} because the separator is not electrically charged during cycling.

Table 5 summarizes the design rules for choosing system parameters required to attain low overall temperature rise and temperature oscillation amplitude in EDLCs during continuous galvanostatic cycling. First, large bulk electrolyte concentration c_∞ and/or diffusion coefficient D_∞ are essential for achieving high ionic conductivity and small heat generation rates. In case of large c_∞ and/or D_∞, although the overall temperature rise is smaller as a consequence of low volumetric heat generation rate, $\dot{q}_{irr}$, the temperature oscillation amplitude ΔT_{rev} is slightly larger due to longer cycle time period t_c. A thick electrode helps in achieving high capacitance but leads to high ESR resulting in rapid increase in device centerline temperature.

Table 5
Summary of the influence of operating conditions, electrode/electrolyte properties and device geometry parameters on area-based capacitance C_A, cycle time period t_c, device centerline temperature $T_{irr}(0, t_0)$, temperature oscillation amplitude ΔT_{rev} $(0, t_0)$ and heat generation rates $\bar{\bar{q}}_{irr}$ and $\bar{\bar{q}}_{rev}$ during galvanostatic cycling.

Increasing →	I_0	σ	aC	D_∞	c_∞	β	α_{ely}	$(\rho c_p)_{ely}$	h	L_e	N
C_A	–	–	↑	↑	↑	–	–	–	–	↑	–
t_c	↓	–	↑	↑	↑	–	–	–	–	↑	–
$T_{irr}(0, t_0)$	↑	–	–	↓	↓	–	↓	↓	↓	↑	↑
$\Delta T_{rev}(0, t_0)$	↓	–	↑	↑	↑	↑	–	↓	–	↓	–
$\bar{\bar{q}}_{irr}$	↑	–	–	↓	↓	–	–	–	–	–	–
$\bar{\bar{q}}_{rev}$	↑	–	–	↓	↓	↑	–	–	–	↑	–

4.2. Dimensionless model analysis

4.2.1. Illustration of scaling analysis

Table 6 summarizes the three sets of input parameters used for scaling analysis. Case I was based on realistic system parameters described by Verbrugge et al. [23]. The ionic conductivity of the electrolyte was assumed to be that of 0.93 M $TEABF_4$ salt in acetonitrile solvent at 25 °C. The input parameters in cases II and III were varied in a way such that all 18 independent dimensionless numbers listed in Eq. (21a) remain constant. Fig. 5(a) illustrates the cell voltage as a function of time t during a single galvanostatic charge/discharge cycle for all three cases. The cell voltage profiles featured different cycle periods for different values of operating current density I_0. Fig. 5(b) plots the dimensionless cell voltage V_{cell}^* versus dimensionless time t^*, and the dimensionless voltage profiles can be observed to overlap one another.

Similarly, Fig. 5(c) and (d) illustrate the dimensional analysis for temperature profiles. The device centerline temperature is shown as a function of time t for all three cases in Fig. 5(c). As expected, higher operating current density I_0 is observed to lead to higher temperature. However, when the results are plotted in terms of dimensionless temperature versus dimensionless time, they all collapse onto a single curve as shown in Fig. 5(d). Therefore, the dimensionless variables $T^*(x^*, t^*)$ and V_{cell}^* (t^*) depend only on the 18 independent dimensionless parameters. The same observations were made for the dimensionless volumetric irreversible and reversible heat generation rates $\dot{q}_{irr}^*$ and $\dot{q}_{rev}^*$ as shown in Figure S4.

4.2.2. Parametric variation of dimensionless numbers

Although all 18 dimensionless parameters are integral to the model, all parameters except Π_1 to Π_7 are essentially ratios of properties

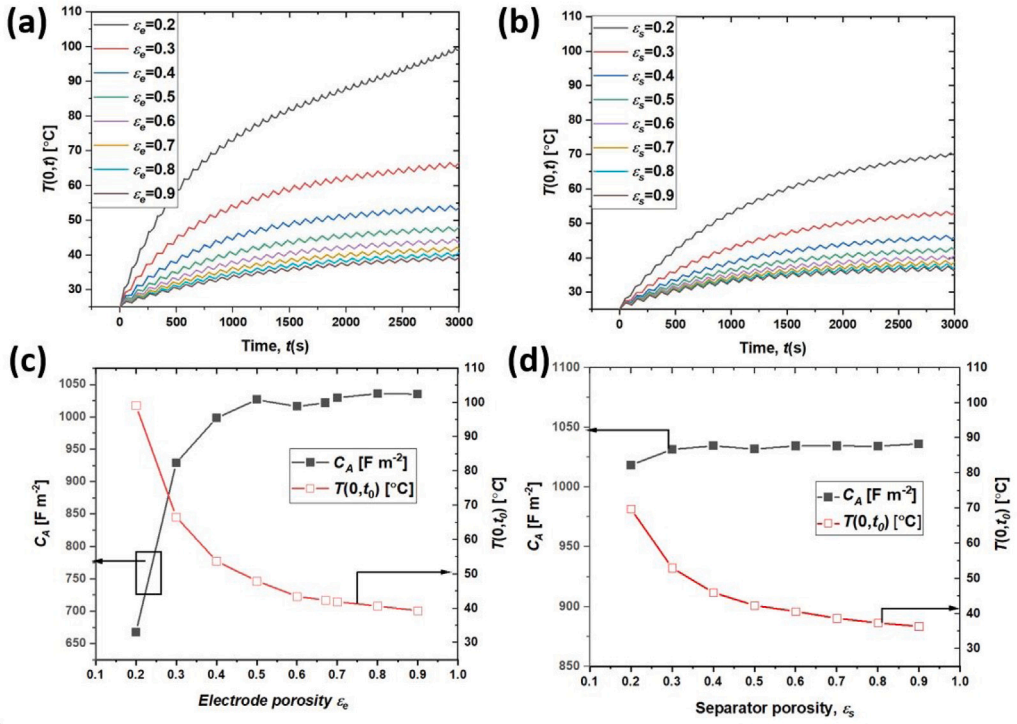

Fig. 4. Computed (a) centerline temperature $T(0,t)$ as a function of time t for ϵ_e ranging from 0.2 to 0.9 while maintaining ϵ_s constant at 0.5, (b) centerline temperature $T(0,t)$ as a function of time t for ϵ_s ranging from 0.2 to 0.9 while maintaining ϵ_e constant at 0.67. Computed (c) area-normalized capacitance C_A and device centerline temperature $T(0,t_0)$ as a function of ϵ_e and (d) area-normalized capacitance C_A and device centerline temperature $T(0,t_0)$ as a function of ϵ_s.

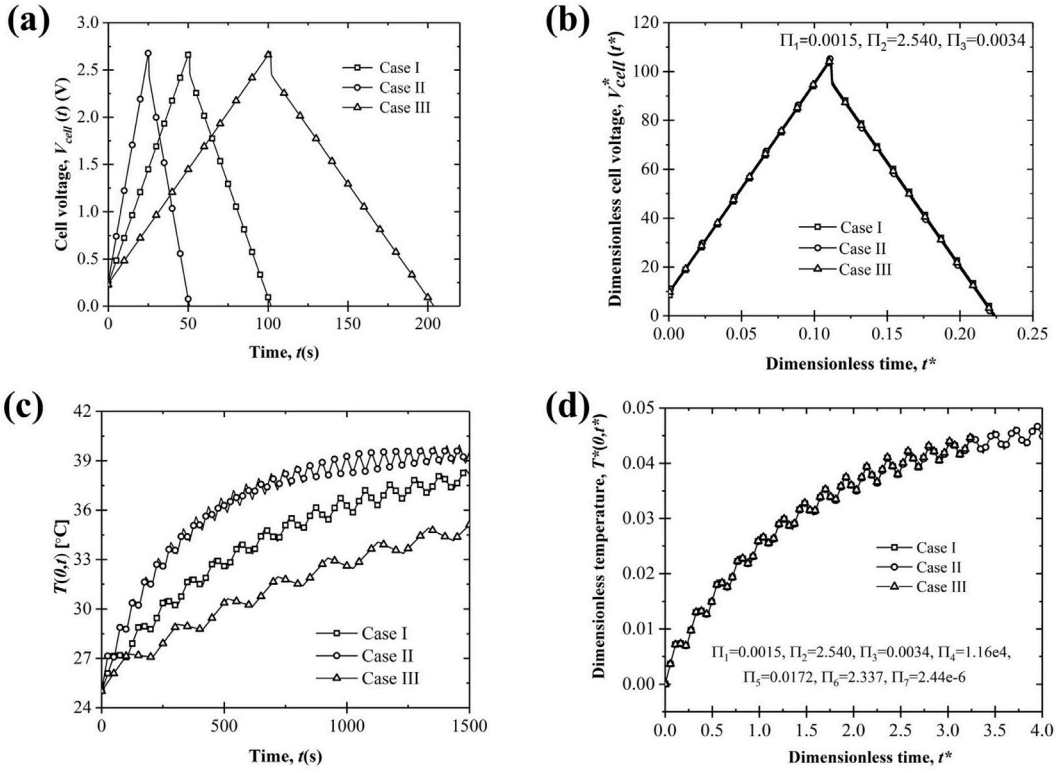

Fig. 5. Computed (a) cell voltage V_{cell} as a function of time t, (b) dimensionless cell voltage V^*_{cell} as a function of dimensionless time t^* during a single galvanostatic charge/discharge cycle for cases I to III (Table 6). Computed (c) device centerline temperature $T(0,t)$ as a function of time t and (d) dimensionless centerline temperature $T^*(0,t^*)$ as a function of dimensionless time t^* for continuous galvanostatic cycling with parameters corresponding to case I to III (Table 6).

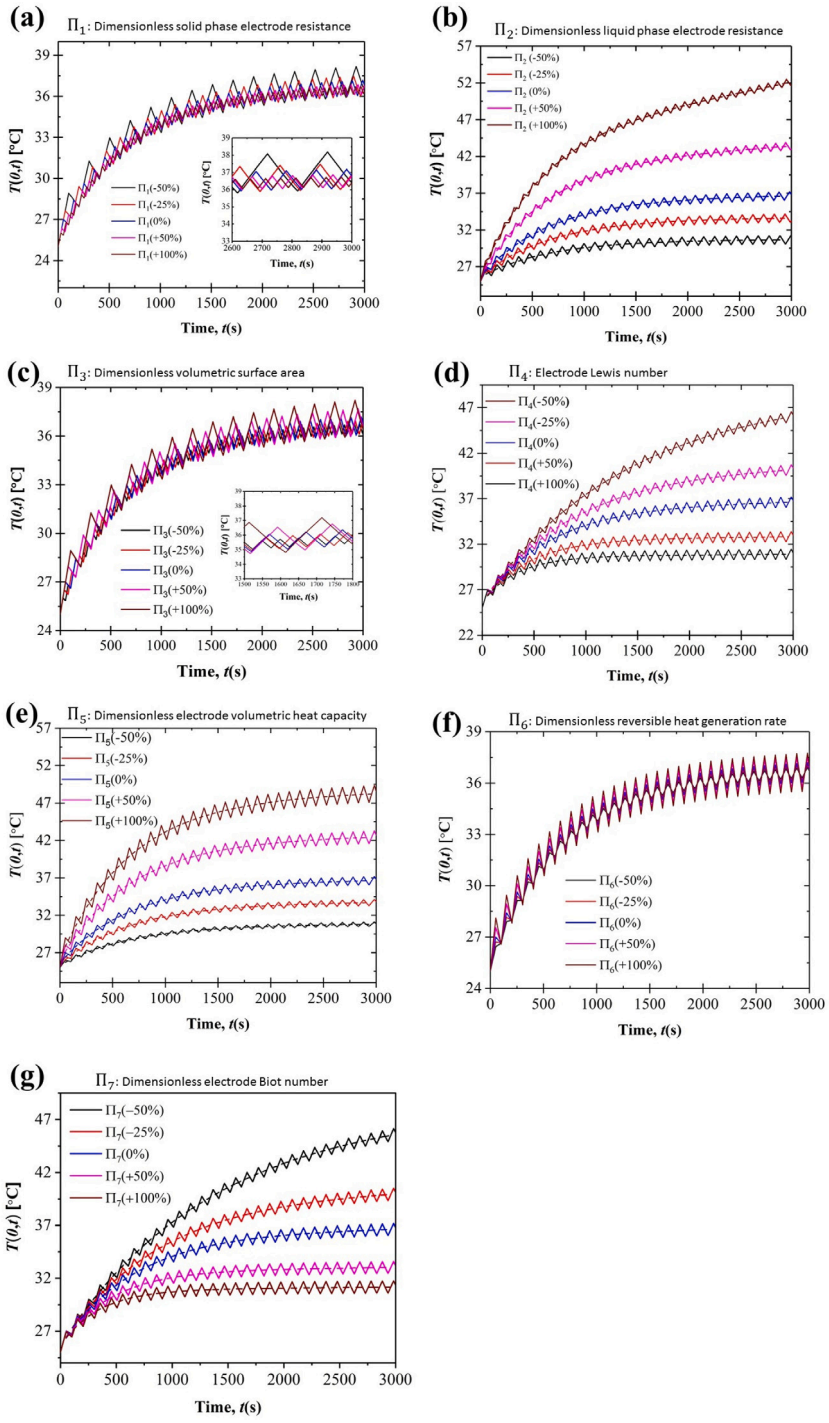

Fig. 6. (a) Variation of device centerline temperature $T(0,t)$ for percentage change in value of dimensionless parameters (a) Π_1, (b) Π_2, (c) Π_3, (d) Π_4, (e) Π_5, (f) Π_6 and (g) Π_7 from their base values. The base values were calculated on parameters listed in Table 8, $\Pi_1 = 0.0015$, $\Pi_2 = 2.540$, $\Pi_3 = 0.0034$, $Le = 1.16 \times 10^4$, $\Pi_5 = 0.0172$, $\Pi_6 = 2.337$ and $\Pi_7 = 2.44 \times 10^{-6}$.

Table 6
Input parameters for Cases I to III used to illustrate the scaling analysis demonstrated in Fig. 5. The dimensionless parameters ϵ_e=0.67, ϵ_s=0.50, L_s^*=0.5, L_{Al}^*=0.4, L_{dev}^*=165, $I_{lm}^* = \pm 1$, $(\rho c_p)^*_{Al}$=1.3, $(\rho c_p)^*_{sep,av}$=0.95, k_{Al}^*=633, $k_{sep,av}^*$=0.77 and σ^*=1.5 × 10^{-9}, Π_1=0.00153, Π_2=2.540, Π_3=0.0034, Le=1.16 × 10^4, Π_5=0.0172, Π_6=2.337 and Π_7=2.44 × 10^{-6} are the same in all three cases.

–	I_0 (A m^{-2})	σ (S m^{-1})	D_∞ (m^2 s^{-1})	k_{Al} (W m^{-1} K^{-1})	k_{elc} (W m^{-1} K^{-1})	k_{ely} (W m^{-1} K^{-1})	k_{sep} (W m^{-1} K^{-1})	h (W m^{-2} K^{-1})
Case I	50	67	1 × 10^{-11}	205	0.649	0.164	0.334	10
Case II	100	134	2 × 10^{-11}	410	1.298	0.328	0.668	20
Case III	25	33	5 × 10^{-12}	103	0.325	0.082	0.167	5

Table 7
Summary of the influence of non-dimensional numbers on area-based capacitance C_A, cycle time period t_c, device centerline temperature $T_{irr}(0, t_0)$, temperature oscillation amplitude ΔT_{rev} $(0, t_0)$ and heat generation rates $\bar{\bar{q}}_{irr}$ and $\bar{\bar{q}}_{rev}$ during galvanostatic cycling.

Increasing →	Π_1	Π_2	Π_3	Π_4	Π_5	Π_6	Π_7
C_A	↓	–	↑	–	–	–	–
t_c	↓	–	↑	–	–	–	–
$T_{irr}(0, t_0)$	–	↑	–	↓	↑	–	↓
$\Delta T_{rev}(0, t_0)$	↓	–	↑	↓	↑	↑	–
$\bar{\bar{q}}_{irr}$	–	↑	–	–	–	–	–
$\bar{\bar{q}}_{rev}$	–	–	–	–	–	↑	–

Table 8
Parameters used in the simulations.

Quantity	Value	Units	Ref.
Carbon electrode thickness L_e	50	μm	[23]
Separator thickness L_s	25	μm	[23]
Current collector thickness L_{Al}	20	μm	[23]
Number of sandwich units N	50	–	–
Volumetric capacitance aC	42	F cm^{-3}	[23]
Initial bulk salt concentration c_∞	0.93	M	[23]
Void volume of carbon electrodes ϵ_e	0.67	–	[28]
Void volume of separator ϵ_s	0.5	–	[28]
Bulk ionic conductivity κ_∞ at c_∞	0.67	mS cm^{-1}	[23]
Solid phase conductivity σ	0.521	mS cm^{-1}	[23]
Base temperature T_0	298	K	–
Upper voltage limit V_{up}	2.7	V	[20]
Total simulation time t_0	3000	s	–
Lower voltage limit V_{low}	0	V	[20]
Aluminum density ρ_{Al}	2700	kg m^{-3}	–
Bulk electrolyte density ρ_{ely}	1205	kg m^{-3}	[20]
Electrode density ρ_{elc}	600	kg m^{-3}	[29]
Separator density ρ_{sep}	492	kg m^{-3}	[29]
Specific heat capacity of aluminum $c_{p,Al}$	900	J kg^{-1} K^{-1}	[29]
Electrical conductivity of aluminum σ_{Al}	37 × 10^6	S/m	
Bulk specific heat capacity of electrolyte $c_{p,ely}$	2141	J kg^{-1} K^{-1}	[20]
Specific heat capacity of electrode $c_{p,elc}$	700	J kg^{-1} K^{-1}	[29]
Specific heat capacity of separator $c_{p,sep}$	1978	J kg^{-1} K^{-1}	[29]
Thermal conductivity of aluminum k_{Al}	205	W m^{-1} K^{-1}	[29]
Bulk thermal conductivity of electrolyte k_{ely}	0.164	W m^{-1} K^{-1}	[29]
Thermal conductivity of electrode k_{elc}	0.649	W m^{-1} K^{-1}	[29]
Thermal conductivity of separator k_{sep}	0.334	W m^{-1} K^{-1}	[29]

and/or dimensions and are less amenable to variation in practice. Hence, we performed parametric analysis only for parameters Π_1 to Π_7. Fig. 6 shows the influence of changes in the value of dimensionless parameters from the base values calculated from dimensional parameters listed in Table 8. Fig. 6(a) shows that the overall temperature rises with time for all values of Π_1. However, the oscillation amplitude in the temperature profiles varies significantly with Π_1 because as Π_1 increases relative to the dimensionless specific capacitance parameter Π_3, the electrode behaves more like a resistor and less like a capacitor. Fig. 6(b) shows that the operating temperature rises more rapidly with time for large values of Π_2. A large Π_2 corresponds to low ionic conductivity or high ESR. Fig. 6(c) shows that an increase in Π_3 leads to rise in oscillation amplitude due to longer cycle time t_c. Fig. 6(d) shows the that for higher values of Π_4 (or Le) the overall temperature rises at a slow pace and reaches steady state value quickly. Fig. 6(e) shows that an exclusive increase in Π_5 leads to rise in both the average temperature and oscillation amplitude. Fig. 6(f) shows that the oscillation amplitude increases with increase in Π_6 although the average temperature remains constant. Fig. 6(g) exhibits that an increase in Π_7 leads to decrease in average operating temperature while keeping oscillation amplitude unchanged.

Table 7 summarizes qualitative changes in the device thermal characteristics $\bar{\bar{q}}_{irr}$, $\bar{\bar{q}}_{rev}$, $T_{irr}(0, t_0)$, ΔT_{rev} caused by variation in the dimensionless model parameters, Π_1 to Π_7. Unlike the dimensional model in which $\bar{\bar{q}}_{irr}$ is a function of multiple parameters (I_0, D_∞ and c_∞), in the case of the dimensionless model, it is a function of only Π_2. Similarly, in the dimensional model, $\bar{\bar{q}}_{rev}$ is a function of I_0, D_∞, c_∞, β and L_e, while in the dimensionless model, it is a function of only Π_6. Thus in summary, scaling analysis of the electrothermal model not only leads to a reduction in the number of independent parameters but also consolidates the dependencies of the volumetric irreversible and reversible heat generation rates.

Table 9
Nomenclature.

Symbol	Description	Units
aC	Capacitance per unit volume	F cm^{-3}
A	Cross-sectional area of the electrode	cm^2
c	Electrolyte concentration	mol m^{-3}
C_A	Capacitance per unit projected area of the electrode	F cm^{-2}
D	Electrolyte diffusion coefficient	m^2 s^{-1}
E_{sp}	Area-specific energy density	J m^{-2}
F	Faraday constant	C
h	Convective heat transfer coefficient at device outer surface	W m^{-2} K^{-1}
$I_{im}(t)$	Time-variant imposed current density	A m^{-2}
I_0	Absolute value of imposed current density	A m^{-2}
k	Thermal conductivity	W m^{-1} K^{-1}
L	Length	m
m	Cell body mass	kg
N	Number of sandwich units in a device	–
Nu	Nusselt number ($\frac{hD}{k_{air}}$)	–
Ra	Rayleigh Number ($\frac{c_{p,air}\rho_{air}^2 g\beta(T-T_{amb})D^3}{\lambda_{air}\mu_{air}}$)	–
P_{sp}	Area-specific power density	W m^{-2}
$\dot{q}$	Local volumetric heat generation rate	W m^{-3}
R_u	Universal gas constant	J mol^{-1} K^{-1}
ESR	Specific equivalent series resistance	Ω m^2
t	Time	s
T_∞	Ambient temperature	K
V	Voltage	V
x	Position along a single sandwich unit	μm
x'	Position along the device consisting of N sandwich units	μm
z_i	Valency	–

Greek symbols

Symbol	Description	Units
ϵ	Porosity	–
κ	Electrolyte ionic conductivity	S m^{-1}
ϕ	Electric potential of a given phase	V
σ	Electrode electrical conductivity	S m^{-1}
(ρc_p)	Volumetric heat capacity	J m^{-3} K^{-1}
β	Entropy constant	J C^{-1}
σ	Electrical conductivity	S m^{-1}

Superscripts and subscripts

Symbol	Description
e	Refers to electrode
s	Refers to separator
∞	Refers to bulk electrolyte
1	Refers to solid phase
2	Refers to electrolyte phase
elc, av	Refers to average over electrode solid and liquid phase
sep, av	Refers to average over separator solid and liquid phase
Al	Refers to aluminum current collector
irr	Refers to irreversible heat generation
rev	Refers to reversible heat generation
dev	Full device consisting of multiple sandwich units
ch	Charge phase
dc	Discharge phase
c	One complete charge/discharge cycle
min	Minimum limit
max	Maximum limit

5. Conclusions

The present study presents a new continuum model based on porous electrode theory for simulating coupled electrochemical and thermal transport during constant-current charging and discharging of EDLCs

composed of identical porous electrodes and binary, symmetric electrolyte. Expressions for irreversible and reversible heat generation rates are rigorously derived. The results compare favorably with past measurements [9,12] both qualitatively and quantitatively. To the best of our knowledge, the present model is the first to comprehensively account for the electrode/electrolyte properties, geometric parameters and operating conditions in evaluating the temperature rise during galvanostatic charge/discharge processes in EDLCs. Scaling analysis performed on the electrothermal model reduced the problem from 29 independent dimensional parameters to 23 physically meaningful dimensionless similarity parameters. Such dimensionless parameters provide a framework that can be used to develop design rules and thermal management strategies for commercial EDLCs.

CRediT authorship contribution statement

Arpan Kundu: Conceptualization, Methodology, Software, Formal Analysis, Writing – original draft, Writing – review & editing, Visualization. **Laurent Pilon:** Methodology, Writing – review & editing. **Timothy S. Fisher:** Conceptualization, Methodology, Supervision, Writing – review & editing, Funding acquisition.

Acknowledgments

The authors thank the U.S. Air Force Office of Scientific Research under the MURI program on Nanofabrication of Tunable 3D Nanotube Architectures (PM: Dr. Joycelyn Harrison, Grant: FA9550-12-1-0037) for support of this work.

Appendix A. Supplementary data

Supplementary material related to this article can be found online at https://doi.org/10.1016/j.jpowsour.2021.230404.

References

[1] K. Maize, A. Kundu, G. Xiong, K. Saviers, T.S. Fisher, A. Shakouri, Electroreflectance imaging of gold-H_3PO_4 supercapacitors. Part I: experimental methodology, Analyst 141 (2016) 1448–1461.
[2] K.R. Saviers, A. Kundu, K. Maize, A. Shakouri, T.S. Fisher, Electroreflectance imaging of gold-H_3PO_4 supercapacitors. Part II: microsupercapacitor ageing characterization, Analyst 141 (2016) 1462–1471.
[3] A. Kundu, T.S. Fisher, Harnessing the thermogalvanic effect of the ferro/ferricyanide redox couple in a thermally chargeable supercapacitor, Electrochim. Acta 281 (2018) 357–369.
[4] A. Kundu, T.S. Fisher, Symmetric all-solid-state supercapacitor operating at 1.5 V using a redox-active gel electrolyte, ACS Appl. Energy Mater. 1 (2018) 5800–5809.
[5] P. Guillemet, Y. Scudeller, T. Brousse, Multi-level reduced-order thermal modeling of electrochemical capacitors, J. Power Sources 157 (1) (2006) 630–640.
[6] H. Gualous, H. Louahlia-Gualous, R. Gally, A. Miraoui, Supercapacitor thermal modeling and characterization in transient state for industrial applications, IEEE Trans. Ind. Appl. 45 (3) (2009) 1035–1044.
[7] O. Bohlen, J. Kowal, D.U. Sauer, Ageing behaviour of electrochemical double layer capacitors: Part II. Lifetime simulation model for dynamic applications, J. Power Sources 173 (1) (2007) 626–632.
[8] M.A. Sakka, H. Gualous, J.V. Mierlo, H. Culcu, Thermal modeling and heat management of supercapacitor modules for vehicle applications, J. Power Sources 194 (2) (2009) 581–587.
[9] J. Schiffer, D. Linzen, D.U. Sauer, Heat generation in double layer capacitors, J. Power Sources 160 (1) (2006) 765–772.
[10] Y. Diab, P. Venet, G. Rojat, Comparison of the different circuits used for balancing the voltage of supercapacitors: Studying performance and lifetime of supercapacitors, in: ESSCAP, Lausanne, Switzerland, 2006, p. on CD.
[11] D.H. Lee, U.S. Kim, C.B. Shin, B.H. Lee, B.W. Kim, Y.-H. Kim, Modelling of the thermal behaviour of an ultracapacitor for a 42-V automotive electrical system, J. Power Sources 175 (1) (2008) 664–668.
[12] H. Gualous, H. Louahlia, R. Gallay, Supercapacitor characterization and thermal modeling with reversible and irreversible heat effect, IEEE Trans. Power Electron. 26 (11) (2011) 3402–3409.
[13] C. Pascot, Y. Dandeville, Y. Scudeller, P. Guillemet, T. Brousse, Calorimetric measurement of the heat generated by a double-layer capacitor cell under cycling, Thermochim. Acta 510 (1) (2010) 53–60.
[14] Y. Dandeville, P. Guillemet, Y. Scudeller, O. Crosnier, L. Athouel, T. Brousse, Measuring time-dependent heat profiles of aqueous electrochemical capacitors under cycling, Thermochim. Acta 526 (1) (2011) 1–8.
[15] O. Munteshari, J. Lau, A. Krishnan, B. Dunn, L. Pilon, Isothermal calorimeter for measurements of time-dependent heat generation rate in individual supercapacitor electrodes, J. Power Sources 374 (2018) 257–268.
[16] O. Munteshari, J. Lau, D. Ashby, B. Dunn, L. Pilon, Effects of constituent materials on heat generation in individual EDLC electrodes, J. Electrochem. Soc. 165 (7) (2018) A1547–A1557.
[17] R. Drummond, D.A. Howey, S.R. Duncan, Low-order mathematical modelling of electric double layer supercapacitors using spectral methods, J. Power Sources 277 (2015) 317–328.
[18] G. Sikha, R.E. White, B.N. Popov, A mathematical model for a lithium-ion battery/electrochemical capacitor hybrid system, J. Electrochem. Soc. 152 (2005) A1682.
[19] A.L. d'Entremont, L. Pilon, Thermal effects of asymmetric electrolytes in electric double layer capacitors, J. Power Sources 273 (2015) 196–209.
[20] A. d'Entremont, L. Pilon, First-principles thermal modeling of electric double layer capacitors under constant-current cycling, J. Power Sources 246 (2014) 887–898.
[21] M. Janssen, R. van Roij, Reversible heating in electric double layer capacitors, Phys. Rev. Lett. 118 (9) (2017) 096001.
[22] A. Wurger, Thermal non-equilibrium transport in colloids, Rep. Progr. Phys. 73 (2010) 126601.
[23] M.W. Verbrugge, P. Liu, Microstructural analysis and mathematical modeling of electric double-layer supercapacitors, J. Electrochem. Soc. 152 (2005) D79–87.
[24] V. Srinivasan, J.W. Weidner, Mathematical modeling of electrochemical capacitors, J. Electrochem. Soc. 146 (1999) 1650–1658.
[25] H. Wang, A. Thiele, L. Pilon, Simulations of cyclic voltammetry for electric double layers in asymmetric electrolytes: A generalized modified Poisson-Nernst-Planck model, J. Phys. Chem. C 117 (2013) 18286–18297.
[26] A. d' Entremont, L. Pilon, Scaling laws for heat generation and temperature oscillations in EDLCs under galvanostatic cycling, Int. J. Heat Mass Transfer 75 (2014) 637–649.
[27] V. Srinivasan, J.W. Weidner, Mathematical modeling of electrochemical capacitors, J. Electrochem. Soc. 146 (1999) 1650–1658.
[28] M.W. Verbrugge, D.R. Baker, B.J. Koch, Mathematical modeling of high-power-density insertion electrodes for lithium ion batteries, J. Power Sources 110 (2) (2002) 295–309.
[29] V. Srinivasan, J.W. Weidner, Mathematical modeling of electrochemical capacitors, J. Electrochem. Soc. 146 (1999) 1650–1658.